RESEARCH ARTICLE

Open Access

Check for updates

Chiral exceptional point and coherent suppression of backscattering in silicon microring with low loss Mie scatterer

Hwaseob Lee[1], Ali Kecebas[2], Feifan Wang[1], Lorry Chang[1], Sahin K. Özdemir[2,3*] and Tingyi Gu[1*]

Abstract

Non-Hermitian systems with their spectral degeneracies known as exceptional points (EPs) have been explored for lasing, controlling light transport, and enhancing a sensor's response. A ring resonator can be brought to an EP by controlling the coupling between its frequency degenerate clockwise and counterclockwise traveling modes. This has been typically achieved by introducing two or more nanotips into the resonator's mode volume. While this method provides a route to study EP physics, the basic understanding of how the nanotips' shape and size symmetry impact the system's non-Hermicity is missing, along with additional loss from both in-plane and out-of-plane scattering. The limited resonance stability poses a challenge for leveraging EP effects for switches or modulators, which requires stable cavity resonance and fixed laser-cavity detuning. Here we use lithographically defined asymmetric and symmetric Mie scatterers, which enable subwavelength control of wave transmission and reflections without deflecting to additional radiation channels. We show that those pre-defined Mie scatterers can bring the system to an EP without post tuning, as well as enable chiral light transport within the resonator. Counterintuitively, the Mie scatterer results in enhanced quality factor measured on the transmission port, through coherently suppressing the backscattering from the waveguide surface roughness. The proposed device platform enables pre-defined chiral light propagation and backscattering-free resonances, needed for various applications such as frequency combs, solitons, sensing, and other nonlinear optical processes such as photon blockade, and regenerative oscillators.

Keywords Non-Hermicity, Exceptional point, Mie scatterers, Microring resonator, Silicon photonics

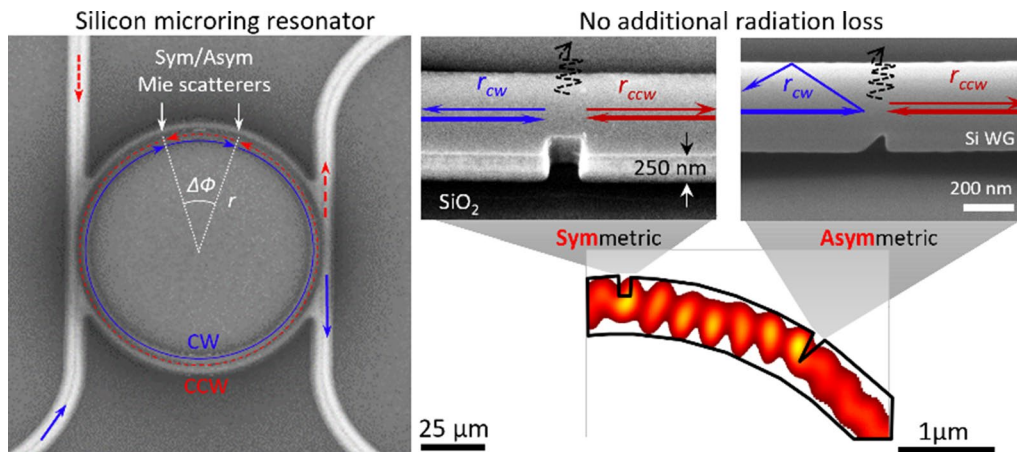*Correspondence:
Sahin K. Özdemir
sko9@psu.edu
Tingyi Gu
tingyigu@udel.edu
Full list of author information is available at the end of the article

Graphical Abstract

1 Introduction

The past decade has witnessed exciting progress in novel functions and processes enabled by the rich physics and the toolbox provided by non-Hermiticity, especially by the emergence of non-Hermitian spectral degeneracies known as exceptional points (EPs) [1–6]. EPs, where both the eigenvalues and the associated eigenvectors of a system coalesce, are radically different from the degeneracies in Hermitian systems, often referred to as diabolic points (DPs), where eigenvectors are orthogonal even when the eigenvalues coalesce. EPs universally occur in all open physical systems (i.e., non-Hermitian) and dramatically affect their behavior, leading to many counterintuitive phenomena such as loss-induced suppression and revival of lasing [7, 8], single-mode lasing [9], directional and mode-selective lasing [10, 11], enhanced response to perturbations [11–14], unidirectional invisibility [15], topological control [16, 17], and chiral perfect absorption [18], just to name a few.

A physical system can be brought to an EP through judicious engineering of the spatial and spectral distribution of loss and/or gain and of the coupling among constituents of the physical system. Non-Hermiticity and the physics associated with EPs cover all physical systems which exchange energy, information, and mass among themselves or with their environments. In coupled optical waveguides and resonators, tuning the coupling strength between the couples with balanced optical gain and loss (i.e., parity-time symmetric systems) [6] and tuning the loss-imbalance of the couples with fixed coupling strength [7, 8] are two commonly used approaches to bring an optical system to an EP.

Another approach that has recently gained more attention is controlling the coupling between the modes of a physical system, such as the frequency-degenerate clockwise (CW) and counterclockwise (CCW) modes in a microring resonator (MRR) or a ring laser [19]. This has been realized using nanotip perturbations [11, 15, 19], Taiji resonators (i.e., resonators with an S-shaped inset) [20], or off-the-chip fiber-loop mirrors [21]. In this paper, we use lithographically defined subwavelength dielectric structures, like individual meta-atoms in metamaterials [22, 23], etched in the same step as MRRs and grating couplers (see Fig. 1a, b). This integrated photonics approach allows us to precisely control the location, size, and geometry of the Mie scatterers, and thus the amplitude, phase and direction of their transmission and reflections. The Mie scatterers embedded in the waveguide are deep subwavelength structures and designed for small reflection (symmetric shape) or deflection at a small angle (asymmetric shape). The energy flow is preserved in the guided modes, and the quality factor (Q) degradation is trivial compared to the nanotip perturbation method and Taiji resonators [20]. Here we show that having a Mie scatterer pair formed with one symmetric and one asymmetric Mie scatterer is sufficient to achieve EP or selected chirality in an MRR. The spatial symmetry of the Mie scatterer maps to the different reflection coefficients for CW and CCW modes. With the Mie scatterers in place, we not only achieve EP but also coherently suppress backscattering in ring resonators caused by the fabrication resulted surface roughness of Rayleigh scatters.
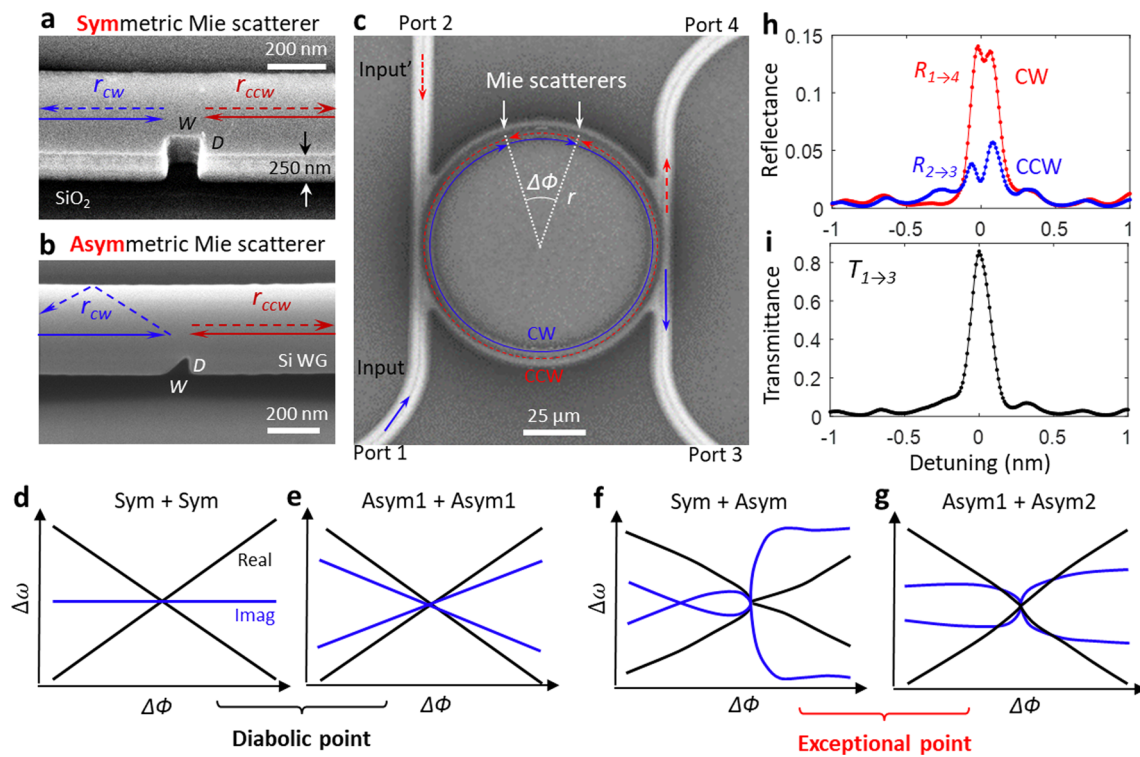
Fig. 1 Exceptional points enabled by a pair of Mie scatterers embedded in channel waveguides and resonators. **a** Scanning electron microscope (SEM) image of a channel waveguide (WG) with a lithographically defined rectangular-shaped symmetric Mie-scatterer on SOI substrate. **b** SEM image of a typical asymmetric Mie scatterer with right triangle shape. **c** A microring resonator (MRR) based add-drop filter with Mie scatterers. The Mie scatterers (**a**, **b**) defined on the ring perimeter control the non-Hermiticity and spectral degeneracy of the MRR state. Depths (*D*) and widths (*W*) are first chosen such that the two Mie scatterers have the same reflectance (Additional file 1: Fig. S1). Then the optical path difference $\Delta\Phi$ between the Mie scatterer pair is tuned to bring the system to an EP or DP. (d, e) A system with a pair of identical symmetric or asymmetric Mie scatterers leads only to a diabolic point (DP) spectral degeneracy (see Additional file 1: Section 2 for detailed derivations). **f**, **g** A combination of one asymmetric and one symmetric Mie scatterer or two non-identical asymmetric Mie scatterers may be tuned to create Eps (see Additional file 1: Section 2 for detailed derivations). The real and imaginary parts of the eigenmodes are plotted in black and blue, respectively. **h** Measured asymmetric reflection spectra (port 1 to 4 and port 2 to 3) and (i) transmission spectrum (port 1 to 3) of the add-drop filter with optimized geometric parameters creating an EP. The asymmetry in the reflection spectra for clockwise (CW) and counterclockwise (CCW) inputs in **h** suggests that the system is at an EP

2 Results

The non-Hermitian system that we consider in this study is an MRR with two lithographically defined Mie scatterers whose reflection coefficients $r_{1cw(ccw)}$ and $r_{2cw(ccw)}$ mediate the inter-modal coupling between the modes [e.g., light in the CW (CCW) mode is reflected into the CCW (CW) mode with r_{1cw} (r_{1ccw}) due to the first Mie scatterer]. Three-dimensional numerical simulation provides direct correlation between the reflection coefficients $r_{1cw(ccw)}$ and the Mie scatterer geometry (Additional file 1: Fig. S1). For a relatively small depth (*D* = 100 nm), the phase of reflection coefficients r_{1cw} (r_{1ccw}) is proportional to the notch width (*W*) [22] (*D* and *W* are marked in Fig. 1a, b). Here, this parameter *D* is carefully selected for introducing sufficient reflection for EP physics studies, but not too large

to degrade the transmission *Q*. The distance *L* between the Mie scatterers leads to a relative phase delay: $\Delta\varphi = 2\pi n_{eff} L/\lambda$ where λ denotes the wavelength of the laser wavelength, n_{eff} corresponding to the effective index of the single mode waveguide. A Mie scatterer in the form of a rectangular (Fig. 1a) has symmetric scattering in the sense that CW to CCW and CCW to CW reflection coefficients are the same (i.e., $r_{cw} = r_{ccw}$). On the other hand, a Mie scatterer in the form of a right triangle (Fig. 1b) defines an asymmetric one where CW to CCW scattering is different than the CCW to CW scattering (i.e., $r_{cw} \neq r_{ccw}$). Also, our numerical studies with practical parameters from the literature show that nanofabrication resulted surface roughness in single mode waveguide leads to asymmetric reflection (Additional file 1: Fig. S2).

Our theoretical analysis shows that two embedded Mie scatterers provide sufficient flexibility to tune the system towards or away from its spectral degeneracies. Only one symmetric Mie scatterer is sufficient to counterbalance the backscattering due to fabrication induced Rayleigh scattering. One can write a general Hamiltonian for such a system (Additional file 1: Section 2):

$$H_2 = \begin{pmatrix} \Omega_0 + \epsilon_{111} + \epsilon_{211} & \epsilon_{112} + \epsilon_{212}e^{-j\Delta\varphi} \\ \epsilon_{121} + \epsilon_{221}e^{j\Delta\varphi} & \Omega_0 + \epsilon_{122} + \epsilon_{222} \end{pmatrix}$$
$$= \begin{pmatrix} \Omega_0 + \chi_1 & \chi_{12} \\ \chi_{21} & \Omega_0 + \chi_2 \end{pmatrix} \quad (1)$$

whose complex-valued elements ϵ_{ikm} describes the coupling strength of the i-th notch-induced scattering into the same ($k = m$) or the counterpropagating ($k \neq m$) mode. The diagonal complex elements ϵ_{i11} and ϵ_{i22} determine the frequency shift and the additional dissipation induced by the Mie scatterers to the CW and CCW modes, respectively. The off-diagonal elements ϵ_{i12} and ϵ_{i21} determine the Mie scatterer induced coupling between CW and CCW modes. Thus, without loss of generality, ϵ_{1km} can be treated as real-valued $\epsilon_{1km} = \epsilon_{1kmr} + i\epsilon_{1kmi}$ where $|\epsilon_{1kmi}| \ll |\epsilon_{1kmr}|$) [22]. The eigenvalues of H_2 are $\omega_\pm = \Omega_0 + (\chi_{21} + \chi_{21})/2 \pm \xi/2$ where $\xi = \sqrt{(\chi_{12} - \chi_{21})^2 + 4\chi_{12}\chi_{21}}$ with the corresponding eigenvectors given as $\psi_\pm = [(\chi_{12} - \chi_{21} \mp \xi)/2\chi_{21} 1]^T$. This system has a spectral degeneracy for $\xi = 0$ which is satisfied when $4\chi_{12}\chi_{21} = -(\chi_{12} - \chi_{21})^2$. The eigenvectors associated with these degenerate eigenvalues are also degenerate and given by $\psi_\pm = [(\chi_{12} - \chi_{21})/2\chi_{21} 1]^T$. Thus, the spectral degeneracies of H_2 with $\xi = 0$ are indeed EPs. Scattering properties of the Mie scatterers that leads to EPs can then be obtained from $\xi = 0$. Since $\chi_{12}\chi_{21}$ is a complex number $\chi_{12}\chi_{21} = \epsilon_{121}\epsilon_{112} + \epsilon_{212}\epsilon_{221} + (\epsilon_{121}\epsilon_{212} + \epsilon_{112}\epsilon_{221})\cos\Delta\varphi + j(\epsilon_{112}\epsilon_{221} - \epsilon_{121}\epsilon_{212})\sin\Delta\varphi$ and $(\chi_{12} - \chi_{21})^2$ is a positive real number, we need to set $\text{Im}(\chi_{12}\chi_{21}) = 0$ and $\text{Re}(\chi_{12}\chi_{21}) = -(\chi_{12} - \chi_{21})^2/4$. The former is satisfied for i) $\Delta\varphi = n\pi$ which leads to $(\epsilon_{121}\epsilon_{112} + \epsilon_{212}\epsilon_{221}) - (\epsilon_{121}\epsilon_{212} + \epsilon_{112}\epsilon_{221}) = -(\chi_{12} - \chi_{21})^2/4$ and for ii) $\epsilon_{112}\epsilon_{221} = \epsilon_{121}\epsilon_{212} = \epsilon'$ leading to $\cos\Delta\varphi = -\frac{1}{2}\left(\frac{(\chi_{12}-\chi_{21})^2}{4\epsilon'} + \frac{\epsilon_{112}^2 + \epsilon_{212}^2}{\epsilon_{112}\epsilon_{212}}\right)$. Based on the geometric symmetry of Mie scatterers, we have categorized their combinations in four groups (Additional file 1: Section 2). Complying with our analysis, their $\Delta\varphi$ dependent exemplary eigenvalues exhibit characteristic behavior of DPs and EPs. A combination of symmetric Mie scatterers or identical asymmetric Mie scatterers only leads to DPs (only eigenvalues coalesce whereas corresponding eigenvectors remain orthogonal) in the MRR (Fig. 1d, e), while

one symmetric one asymmetric Mie scatterer or by two non-identical asymmetric Mie scatterers lead to an EP (both eigenvalues and corresponding eigenvectors coalesce), if the inter-Mie scatterer distance is properly adjusted (Fig. 1f, g) (Additional file 1: Section 2).

Following the theoretical analysis, we fabricated a set of MRRs with embedded symmetric and asymmetric Mie scatterers on a silicon-on-insulator (SOI) substrate (Fig. 1a, b). A MRR enhanced directionality is characterized with an add-drop design, where the symmetric ports support both CW and CCW excitations (Fig. 1c). Light input in Port 1 (Port 2) excites the CW (CCW) mode, and the reflected optical powers are collected in Port 4 (Port 3). The high contrast between the reflections from CW and CCW excitations indicate the system operates near an EP (Fig. 1h). Using the transmission spectra at the drop-port we have estimated the Q of the fabricated MRR as ~ 15,000 (Fig. 1i).

Figure 2 illustrates the design principle of the Mie scatterers enabled EP system. We consider the design is successful when intracavity field becomes chiral (i.e., maximal chirality is achieved when field in CW/CCW direction is zero while the field in the other direction is maximal). In order to achieve this, we used a Smith Chart based 'optical impedance matching' approach where EPs and hence maximal chirality occurs at the intersection of the trajectories of the reflection coefficients of Mie scatterers constructed by tuning the dimensions of the Mie scatterers and the distance between them. At each crossing point, the effective reflections cancel out in the backward or the forward direction. With a symmetric-asymmetric pair of Mie scatterers, the reflection coefficient trajectories (or optical smith chart) change with the width W of the symmetric Mie scatterer and the distance L between the Mie scatterers (Fig. 2a). Figure 2b illustrates the case for two asymmetric Mie scatterers. Figures 2c, d show the mode-splitting $\xi = \Delta\omega$ as a function of the phase relative phase of $\Delta\varphi$, with W value satisfying impedance matching process in Fig. 2a, b. Emergence of EPs, identified by $\xi = |\Delta\omega| = 0$ and the coalesce of both the real and imaginary parts of the reflection $\Delta\omega$, is clearly seen.

One of the challenges in fabricating high-Q resonator systems is mode-splitting arising from intermodal coupling, induced by the distributed nanometer-scale scatters formed during the waveguide etching process. Presence of mode-splitting implies the formation of a standing-wave in the resonator, and suppressing such inter-modal coupling can results in improved Q. In order to check the feasibility of our method to overcome this challenge, we studied a resonator system with randomly distributed scattering centers (similar
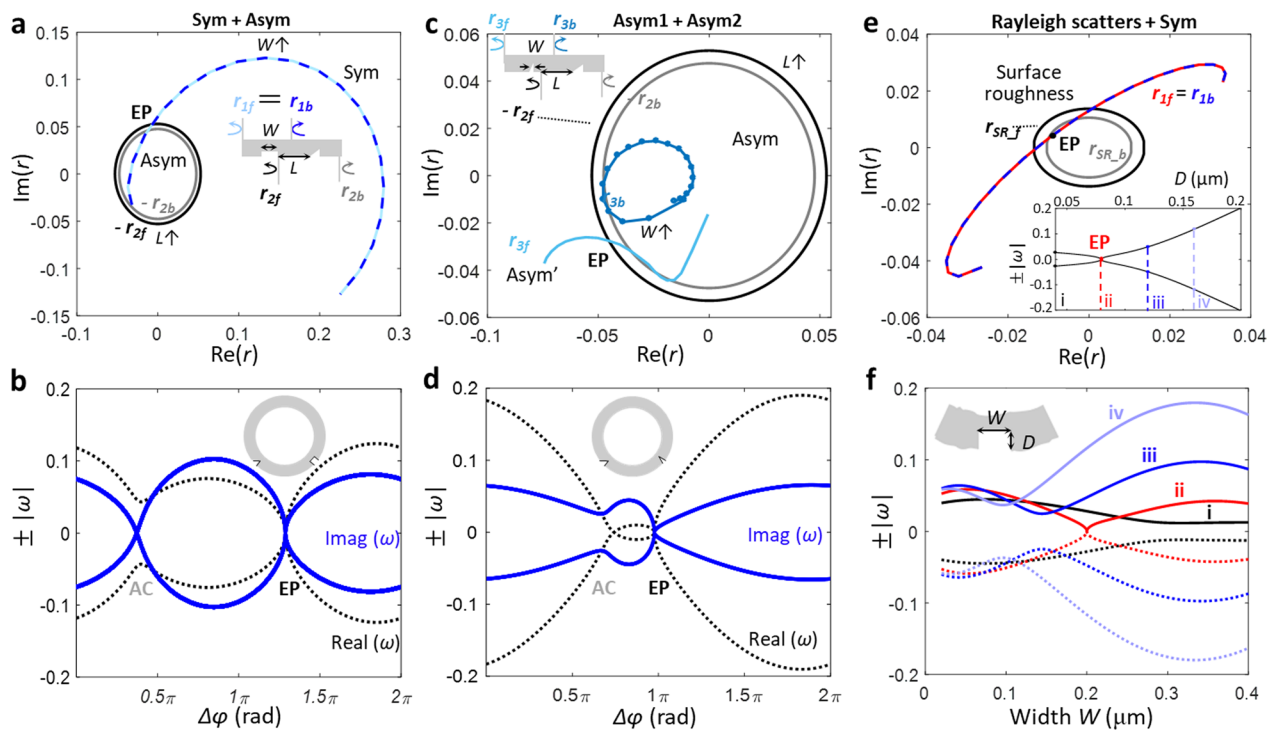
Fig. 2 Optical impedance matching towards EP. **a** Complex reflectivity of a Mie scatterers embedded channel waveguide with forward (r_f) and backward (r_b) excitation. The symmetric rectangular shaped Mie scatterers with dimensions $D = 200$ nm, $W = 20 \sim 400$ nm have the same r_f (light blue solid curve) and r_b (blue dashed curve). An asymmetric (right triangle) Mie scatterer with dimension $D = 200$ nm and $W = 140$ nm has different r_f (black curve) and r_b (gray). Distance L between the Mie scatterers is varied in the range $L = 0 \sim \lambda$. **b** Asymmetric reflectivity of a channel waveguide with two asymmetric (i.e., right triangle) Mie scatterers. Blue curves: $D_{Asym} = 160$ nm, $W_{Asym} = 20$ to 400 nm. Black and grey curves: $D_{Asym} = 200$ nm, $W_{Asym} = 140$ nm. The optical path length between the input point and the scatter varies from 0 to λ. (c,d), The real (black dashed curve) and imaginary (blue dots) parts of the eigenvalues versus optical path length $\Delta\Phi$ (**c**) between a symmetric and an asymmetric Mie scatterers, and (**d**) between two nonidentical asymmetric Mie scatterers. W of the symmetric Mie scatterer in **c** is taken as 80 nm, and that of the asymmetric Mie scatterer in **d** is taken as 240 nm. The dimensions of the Mie scatterers used in **c** and **d** are chosen from the intersection points of reflectivity plots in **a** and **b**. EP: exceptional point; AC: avoided crossing. **e** Complex reflectivity of a channel waveguide with an embedded symmetric Mie scatterer (red: forward scattering; blue: backward scattering) and that of a channel waveguide with surface roughness (black: forward scattering; gray: backward scattering). The Mie scatterer depth D is fixed at 80 nm, and its width W is varied from 20 to 400 nm. The reflectivity trajectory of the Mie-scatterer overlaps with the reflectivity of the channel waveguide with sidewall surface roughness ($L_c = 100$ nm, $\sigma = 10$nm) at $W = 180$ nm. Inset: Magnitude of the complex frequency splitting $\pm|\omega|$ versus D of the Mie-scatterer with $W = 180$ nm defined on the perimeter of the MRR. EP emerges at D value where $\pm|\omega| = 0$. (**f**) $\pm|\omega|$ versus W of the Mie-scatterer with D equals to 30 nm (black), 80 nm (red), 120 nm (blue) and 160 nm (light blue)

to sidewall roughness which may form due to fabrication imperfections etc.) and a single symmetric Mie scatterer. The sidewall roughness was simulated by randomly distributed Rayleigh scatters whose depth σ ranged in the range of 5–50 nm with the correlation length (L_c) taken larger than 50 nm [24] (Additional file 1: Fig. S2).We found that EPs emerge and hence a transition from standing wave to traveling wave is established when the width W and the depth D of the Mie scatterer is tuned to achieve impedance matching between the reflections from the designed Mie scatterer and fabricated induced random Rayleigh scatterers (Fig. 2c, f). This finding provides a route to suppress inter-modal scattering by embedding judiciously

engineered notch geometry in ring resonators. We note here that one can certainly use reflow techniques, although not all the materials can be re-flowed by heating and melting, to reduce the average size of scattering centers but even in such cases of small scatterers intermodal scattering exists and leads to mode splitting for high-Q resonators [25]. Also, high temperature process beyond 300 °C is prohibited in active silicon devices with doping and metal contacts, as it leads to the device failure.

To experimentally demonstrate the design concept, we fabricated a set of MRRs with same surface roughness levels but each with a symmetric Mie scatterer of different width W chosen in the range 0–420 nm. The depth
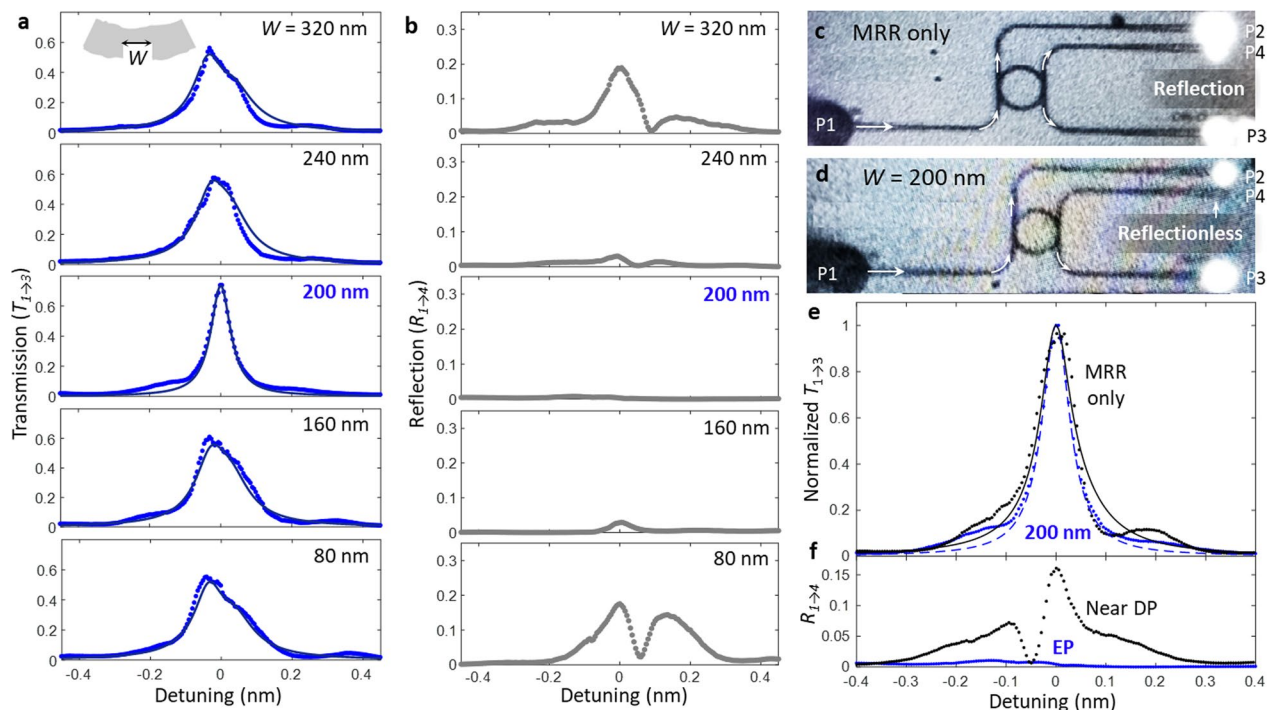
Fig. 3 Experimental demonstration of suppressed reflection and improved quality factor in MRRs by engineering geometry of the Mie scatterer. **a** Transmission ($T_{1\rightarrow3}$) and (**b**) reflection spectra ($R_{1\rightarrow4}$) of the MRR in add-drop configuration as shown in Fig. 1 for a Mie scatterer with $D=100$ nm and $W=80$ nm, 160 nm, 200 nm, 240 nm, and 320 nm (top to bottom). The devices with different W are fabricated in the same run to make sure that they are affected in the same way during the fabrication (e.g., similar fabrication imperfections and sidewall roughness). $R_{1\rightarrow4}$ becomes zero, suggesting the emergence of an EP, at $W=200$ nm in good agreement with the design process in Fig. 2. **c** Infrared camera captured top view of a ring resonator without and (**d**) with the Mie scatterer ($W=200$ nm, $D=100$ nm). A single mode fiber launches light through the grating coupler connected to port 1. The ring resonator without the Mie scatterer experiences intermodal scattering due to sidewall roughness which results in strong reflection signal at port 4 (reflection port), which is suppressed in **d**. $T_{1\rightarrow3}$ and (f) $R_{1\rightarrow4}$ of the MRRs shown in the **c** (black) and **d** (blue), respectively. Dots: experimental data. Curves: CMT fits

D of the Mie scatterer was chosen as 100 nm to match its reflectance (Additional file 1: Fig. S1) with the one from the surface roughness (Additional file 1: Fig. S2). Figure 3a, b show the measured transmission and corresponding reflection spectra in the drop and add ports, for this set of MRRs. The geometry dependent parameters are extracted by fitting the coupled mode theory (CMT) model to the measured spectra (solid curves in Fig. 3a). Change in the reflection and transmission spectra obtained for Mie scatterers of different W are clearly seen. With notch width away from EP condition, the absence of observable split-mode spectra in the transmission and the presence of non-zero reflection implies that inter-modal coupling due to surface roughness is present in the system. Moreover, the observation that the resonances have deviated from a Lorentzian form and present a broadened form signals the presence of inter-modal coupling. This situation is completely erased for the Mie scatterer with $W=200$ nm, which is the transmission spectrum presents a Lorentzian line shape and the reflection does not present a resonance and is zero. This

corresponds to maximum rectification, which is referred to as the difference between the transmission and reflection spectra, implying that this Mie scatterer completely compensates the inter-modal scattering induced by surface roughness as expected from our theoretical analysis.

Suppression of backscattering is confirmed by the infrared camera captures of the reflected light in port 4 (reflection port) of the MRRs (Fig. 3c) which clearly show the presence of a bright spot at port 4 of the MRR without the meta-atom and the dark spot at port 4 of the MRR with the embedded meta-atom (Fig. 3d). The transmission (Fig. 3e) and reflection spectra (Fig. 3f) of MRRs with and without the meta-atom of $W=200$ nm shows that both MRRs have similar transmission but significantly differing reflection spectra. The measured Q_t increases from 16,300 ($W=0$ nm) to 21,300 ($W=200$ nm). Presence of reflection for the MRR without the meta-atom indicates the simultaneous presence of both the CW and CCW light inside the resonator due to scatterer-induced modal coupling although this does not reflect itself as mode-splitting in the transmission
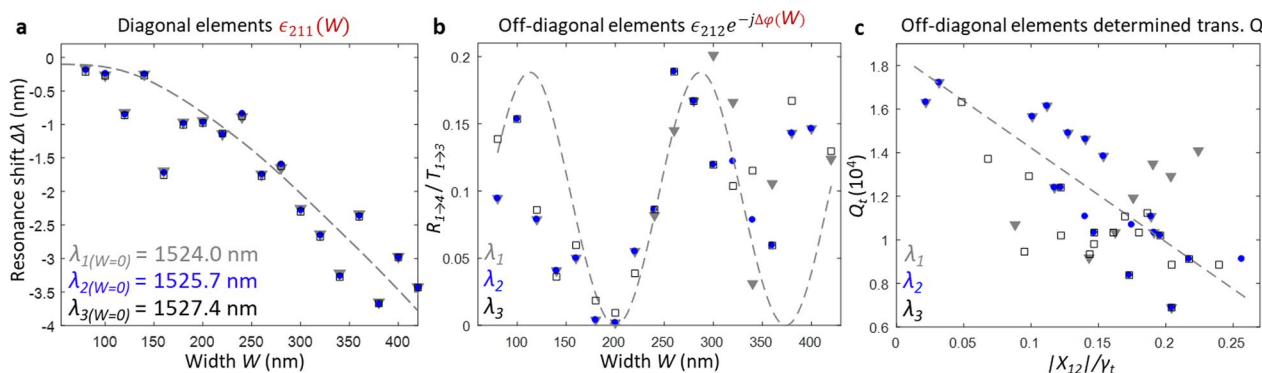
Fig. 4 Measured dependence of diagonal and off-diagonal elements in the non-Hermitian Hamiltonian (Eq. 1) on the Mie scatterer width. **a** Resonance wavelength detuning versus the notch width W for three adjacent modes marked as $\lambda_{1\text{-}3}$, with the incremental step of $\Delta W = 20$ nm. The resonance wavelength of the modes is between 1520 and 1530 nm. **b** Comparison of measured and modeled (dashed curve) on-resonance transmission and reflection versus designed Mie scatterer width W. The grey curve is CMT mode prediction. **c** Total quality factor extracted from the transmission spectra ($T_{1\rightarrow3}$) versus normalized forward scattering coefficient $|X_{12}|/\gamma_t$ (extracted from the normalized reflection $R_{1\rightarrow4}/T_{1\rightarrow3}$). The grey triangles, blue dots and black squares are experimental data for the three adjacent modes separated by 2 nm free spectral range. The dashed grey curve and line in a and c are eye guiders. The grey curve in **b** is predicted by CMT model

spectra. Absence of reflection for the MRR with the Mie scatterer suggests that the system is at an EP and scattering from the Mie scatterer and the backscattering induced by the sidewall scatterers destructively interfere, eliminating the CCW propagating mode. We found that the Mie scatterer with $W = 200$ nm resulted in minimal back-reflection, suggesting a good agreement with our design strategy to approach the EP degeneracy. By comparing to the MRR with surface roughness only, we estimated the reflection parameters of the Mie scatterer as $r_{1b} = 19.67e^{j(-1.14)}$ GHz and $r_{1f} = 17.57e^{-j2.54}$ GHz from the experimental data. Performing model fitting using CMT yields radiation loss $\gamma_o = 13.32$ GHz (i.e., $Q_{in} = 78{,}360$) and the coupling losses as 39.96 GHz for CW and CCW modes (Additional file 1: Section 4).

From the measured transmission spectra, we extract the resonance wavelengths at multiple adjacent resonances separated by the free spectral range of ~ 2 nm. The resonance shift versus the Mie scatterer geometry almost the same among the three modes (Fig. 4a). Their deviation from the trend (dashed curve) is attributed to the fabrication variation. The resonance shift is proportional to the W dependent diagonal element ϵ_{211} in Eq. (1), which comes along with the tuning of off-diagonal elements. We also extracted the off-diagonal element ($\epsilon_{212}e^{-j\Delta\varphi(W)}$) from the reflection spectra. The ratio of the reflection to the transmission at zero-detuning defined as $|\chi_{12}| = \frac{\gamma_t}{2}\sqrt{\frac{R_{1\rightarrow4}}{T_{1\rightarrow3}}}$ where γ_t is the total loss rate of the MRR is depicted for these modes in Fig. 4b. We see that $|\chi_{12}|$ obtained for these modes are very similar to each other and agree well with the theoretical predicted dependence on W (Additional file 1: Section 3). These suggest that the system is not sensitive to dispersion.

Finally, we experimentally obtained the total quality factor (Q_t) from the transmission and found that it linearly decreases with the χ_{12} extracted from the measured reflection spectra, for the three modes mentioned above. Figure 4c shows the correlation between transmission and reflection at the resonance frequency, as a function of width W. The enhancement of Q_t in the transmission spectra (1.3 times in Fig. 3e for the given Rayleigh scattering and 3 times between the maximum and minimum in Fig. 4c) is difficult to be captured in previous studies which used nanotips for EP but it can be systematically studied in our the integrated photonic MRR. We note that this robustness enabled by the integrated photonic platform is highly desirable in EP studies [26, 27].

3 Discussion

In conclusion, we have shown that non-Hermiticity in optical resonators can be engineered by designing and lithographically patterning Mie scatterers into the resonator. The amplitude and phase of the Mie scatterer's reflectivity can be deterministically controlled by its D and W, respectively [22]. The Mie scatterers embedded in MRRs offer a unique low loss approach because the perturbed propagation vector still satisfies the total internal reflection for the guided modes in the resonator. This has not only allowed us to bring a system to an EP but also allowed us to go beyond the fabrication induced Rayleigh scattering integrated photonic high-Q MRR and microdisk resonators [32, 33]. Detailed performance matrix comparison of this predefined EP approach and the ones in literature is summarized in Additional file 1: Section 5.

Non-Hermicity is ubiquitous in integrated photonic resonators but not well formulated, neither of their

chirality [28–36]. In all the devices, the random wave-guide sidewall roughness introduces different off-diagonal elements (Fig. S2) in the Hamiltonian and leads to unexpected mode-splitting in MRR [28, 29, 34, 35]. Counterintuitively, here we show that additional 'defect' of the Mie scatterer can further enhances Q ($\sim 10^5$) by suppressing the coherent backscattering. This post-tuning free chiral integrated photonic system opens many opportunities towards EP-enhanced sensors, optomechanical and parametric nonlinear interactions [36, 37], and lasing. It also helps to build photonic structures with asymmetric reflection profiles and backscattering-free resonators for various applications such as frequency combs, solitons, sensing, and other nonlinear optical processes such as photon blockade, and regenerative oscillators. The lithographically defined platform enables deterministic control of light propagation, toward the exploration of EP physics coupled with parametric and free-carrier dynamics in silicon MRRs.

Beyond opening a new direction for chiral silicon photonics, the combined theoretical analysis and experimental results that presented in this work also advances the knowledge of EP [38]. First, it reveals the critical role of spatial asymmetry of the nanotip and Mie scatterers for bringing the system towards EP. Second, scatter geometry-controlled pathway of driving the non-Hermitian system towards and away from an EP is illustrated in details. Third, the mechanically stable system allows reliable comparison between transmission and reflection spectra for the perturbed micro-resonator, which reveals the nanotip/scatter's contribution to the diagonal terms. Forth, enhancement of the empirical Q extracted from the transmission spectra are demonstrated for the first time.

4 Materials and methods
4.1 Sample fabrication
The MRRs are fabricated on a SOI substrate from Soitec, having a 250 nm silicon layer and 3 μm buried oxide layer. The substrates initially undergo pre-cleaning in organic solvents followed by Nanostrip at 80 °C to remove any particulate matter or contaminants on the surface. The structures are patterned in AR-P-CSAR 6200.09 positive E-beam resist (thickness: ~ 275 nm) by Vistec EBPG5200 electron beam lithography system with 100 kV acceleration voltage. A base dosage is adjusted to be ~ 120 $\mu c^2/cm^2$ for the multi-pass writing to minimize the field stitching error, followed by a proper proximity effect correction. During the electron beam lithography, a ring waveguide is broken down into a polygon path, resulting in different number of actual exposure dots around the

path. The pattern is developed using AR-600-546 developer solution. Our chip is then etched by inductively coupled plasma (ICP) Etching tool using Fluorine-based chemistry, in which Sulfur hexafluoride (SF_6) gas is used to mainly etch the silicon while Octafluorocyclobutane (C_4F_8) gas is carefully adjusted with respect to SF_6 gas for the passivation during etching, preventing a thin E-beam resist erosion (C_4F_8:SF_6 = 1:1). An intermittent plasma asher step is performed to remove any residual resist. A 0.3 mμ thick silicon dioxide is deposited by plasma enhanced chemical vapor deposition (PECVD) at 300 °C and 1.4 Torr pressure using silane (SiH_4) and Nitrous oxide (N_2O) as precursor gases.

4.2 Optical measurements
A tunable laser in telecommunication C band sends the TE polarized light to the on-chip grating coupler through a polarization controller. The output power is monitored by a Newport InGaAs photodiode (818-IG-L-FC/DB) and an optical power meter (1830-R-GPIB).

4.3 Numerical simulations
A three-dimensional finite-difference-time-domain (3D FDTD) method simulates the optical field distribution, transmission, and reflection coefficients. The conformal mesh with spatial resolution less than 1/10 of the local feature size is applied for FDTD simulation.

Supplementary Information

Additional file 1: Section S1. Directional reflection coefficients in notch embedded single mode waveguide. **Figure S1**. Width (W) and Depth (D) determined reflectance for symmetric and asymmetric Mie scatterers. **Figure S2**. Distributed Rayleigh scatterer induced asymmetric reflection. **Section S2**: Mie scatterer defined non-Hermicity in MRRs. **Figure S3**. Mie scatterer combinations and resulting non-Hermitian states. **Figure S4**. Mie scatterer geometry defined non-Hermitian states. **Section S3**: Empirical model for extracting the experimental parameters. **Figure S5**. Illustration for the coupled harmonic oscillator model. **Figure S6** χ_{12} phase dependent spectra. **Section S4**: Interpretation of the experimental data. **Figure S7**. Measurement results of the set of MRRs with varying notch width. **Section S5**: Comparison with other works. **Table S1**: Nano/micro-photonic structures for back reflection suppression.

Author contributions
HL and TG conceived the idea. HL, SKO and TG developed the experimental plan. HL designed and fabricated the devices. HL and FW conducted the device characterizations. HL and AK performed the detailed modeling and results analysis, supervised by SK, HL and TG wrote the manuscript with inputs from the other coauthors. All authors read and approved the final manuscript.

Availability of data and materials

The datasets used and/or analyzed during the current study are available from the corresponding author on reasonable request.

Declarations

Competing interests

All other authors declare they have no competing interests.

Author details

[1]Department of Electrical and Computer Engineering, University of Delaware, Newark, DE 19716, USA. [2]Department of Engineering Science and Mechanics, Pennsylvania State University, University Park, PA 16802, USA. [3]Materials Research Institute, Pennsylvania State University, University Park, PA 16802, USA.

References

1. ŞK. Özdemir, S. Rotter, F. Nori, L. Yang, Parity–time symmetry and exceptional points in photonics. Nat. Mater. **18**, 783–798 (2019)
2. M.-A. Miri, A. Alù, Exceptional points in optics and photonics. Science **363**, eaar7709 (2019)
3. R. El-Ganainy, K.G. Makris, M. Khajavikhan, Z.H. Musslimani, S. Rotter, D.N. Christodoulides, Non-Hermitian physics and PT symmetry. Nat. Phys. **14**, 11–19 (2018)
4. L. Feng, R. El-Ganainy, L. Ge, Non-Hermitian photonics based on parity–time symmetry. Nat. Photonics **11**, 752–762 (2017)
5. R. El-Ganainy, M. Khajavikhan, D.N. Christodoulides, S.K. Ozdemir, The dawn of non-Hermitian optics. Commun. Phys. **2**, 1–5 (2019)
6. B. Peng, ŞK. Özdemir, F. Lei, F. Monifi, M. Gianfreda, G.L. Long, S. Fan, F. Nori, C.M. Bender, L. Yang, Parity–time-symmetric whispering-gallery microcavities. Nat. Phys. **10**(5), 394–398 (2014)
7. A. Guo, G.J. Salamo, D. Duchesne, R. Morandotti, M. Volatier-Ravat, V. Aimez, G.A. Siviloglou, D.N. Christodoulides, Observation of P T-symmetry breaking in complex optical potentials. Phys. Rev. Lett. **103**, 093902 (2009)
8. H. Hodaei, M.-A. Miri, M. Heinrich, D.N. Christodoulides, M. Khajavikhan, Parity-time-symmetric microring lasers. Science **346**, 975–978 (2014)
9. M.-A. Miri, P. LiKamWa, D.N. Christodoulides, Large area single-mode parity-time-symmetric laser amplifiers. Opt. Lett. **37**, 764–766 (2012)
10. L. Chang, X. Jiang, S. Hua, C. Yang, J. Wen, L. Jiang, G. Li, G. Wang, M. Xiao, Parity–time symmetry and variable optical isolation in active–passive-coupled microresonators. Nat. Photonics **8**, 524–529 (2014)
11. E. Lafalce, Q. Zeng, C.H. Lin, M.J. Smith, S.T. Malak, J. Jung, Y.J. Yoon, Z. Lin, V.V. Tsukruk, Z.V. Vardeny, Lasing modes in coupled colloidal quantum dot microdisk pairs using a non-Hermitian exceptional point. Nat. Commun. **10**, 561 (2019)
12. J.-H. Park, A. Ndao, W. Cai, L. Hsu, A. Kodigala, T. Lepetit, Y.-H. Lo, B. Kanté, Symmetry-breaking-induced plasmonic exceptional points and nanoscale sensing. Nat. Phys. **16**(4), 462–468 (2020)
13. Y.-H. Lai, Y.-K. Lu, M.-G. Suh, Z. Yuan, K. Vahala, Observation of the exceptional-point-enhanced Sagnac effect. Nature **576**, 65–69 (2019)
14. H. Hodaei, A.U. Hassan, S. Wittek, H. Garcia-Gracia, R. El-Ganainy, D.N. Christodoulides, M. Khajavikhan, Enhanced sensitivity at higher-order exceptional points. Nature **548**(7666), 187–191 (2017)
15. A.Ø. Svela, J.M. Silver, L.D. Bino, S. Zhang, M.T.M. Woodley, M.R. Vanner, P. Del'Haye, Coherent suppression of backscattering in optical microresonators. Light Sci. Appl. **9**, 1–8 (2020)
16. H. Xu, D. Mason, L. Jiang, J.G. Harris, Topological energy transfer in an optomechanical system with exceptional points. Nature **537**, 80–83 (2016)
17. J. Doppler, A.A. Mailybaev, J. Böhm, U. Kuhl, A. Girschik, F. Libisch, T.J. Milburn, P. Rabl, N. Moiseyev, S. Rotter, Dynamically encircling an exceptional point for asymmetric mode switching. Nature **537**, 76–79 (2016)
18. M.S. Ergoktas, S. Soleymani, N. Kakenov, K. Wang, T.B. Smith, G. Bakan, S. Balci, A. Principi, K.S. Novoselov, S.K. Ozdemir, C. Kocabas, Topological engineering of terahertz light using electrically tunable exceptional point singularities. Science **376**, 184–188 (2022)
19. B. Peng, ŞK. Özdemir, M. Liertzer, W. Chen, J. Kramer, H. Yılmaz, J. Wiersig, S. Rotter, L. Yang, Chiral modes and directional lasing at exceptional points. Proc. Natl. Acad. Sci. **113**, 6845–6850 (2016)
20. W.E. Hayenga, M. Parto, J. Ren, F.O. Wu, M.P. Hokmabadi, C. Wolff, R. El-Ganainy, N.A. Mortensen, D.N. Christodoulides, M. Khajavikhan, Direct generation of tunable orbital angular momentum beams in microring lasers with broadband exceptional points. ACS Photonics **6**, 1895–1901 (2019)
21. S. Soleymani, Q. Zhong, M. Mokim, S. Rotter, R. El-Ganainy, ŞK. Özdemir, Chiral and degenerate perfect absorption on exceptional surfaces. Nat. Commun. **13**, 1–8 (2022)
22. Z. Wang, T. Li, A. Soman, D. Mao, T. Kananen, T. Gu, On-chip wavefront shaping with dielectric metasurface. Nat. Commun. **10**, 3547 (2019)
23. Q. Zeng, E. Lafalce, C.H. Lin, M.J. Smith, J. Jung, Y. Yoon, Z. Lin, V.V. Tsukruk, Z.V. Vardeny, Control of whispering gallery modes and PT-symmetry breaking in colloidal quantum dot microdisk lasers with engineered notches. Nano Lett. **19**, 6049–6057 (2019)
24. T. Wang, Z. Zhang, F. Liu, Y. Tong, J. Wang, Y. Tian, M. Qiu, Y. Su, Modeling of quasi-grating sidewall corrugation in SOI microring add-drop filters. Optics Commun. **282**, 3464–3467 (2009)
25. C. Bellegarde, E. Pargon, C. Sciancalepore, C. Petit-Etienne, V. Hughes, J.-M. Hartmann, P. Lyan, Improvement of sidewall roughness of sub-micron silicon-on-insulator waveguides for low-loss on chip links. In Silicon Photonics XII **10108**, 1010816 (2017)
26. A. Hashemi, S.M. Rezaei, S.K. Özdemir, R. El-Ganainy, New perspective on chiral exceptional points with application to discrete photonics. APL Photonics **6**, 040803 (2019)
27. Q. Zhong, J. Ren, M. Khajavikhan, D.N. Christodoulides, ŞK. Özdemir, R. El-Ganainy, Sensing with exceptional surfaces in order to combine sensitivity with robustness. Phys. Rev. Lett. **122**, 153902 (2019)
28. X. Zhang, Q.T. Cao, Z. Wang, Y.X. Liu, C.W. Qiu, L. Yang, Q. Gong, Y.F. Xiao, Symmetry-breaking-induced nonlinear optics at a microcavity surface. Nat. Photonics **13**, 21–24 (2019)
29. S. Kim, K. Han, C. Wang, J.A. Jaramillo-Villegas, X. Xue, C. Bao, Y. Xuan, D.E. Leaird, A.M. Weiner, M. Qi, Dispersion engineering and frequency comb generation in thin silicon nitride concentric microresonators. Nat. Commun. **8**, 372 (2017)
30. D. Dai, Y. Tang, J.E. Bowers, Mode conversion in tapered submicron silicon ridge optical waveguides. Opt. Express **20**, 13425–13439 (2012)
31. H. Lee, T. Kananen, A. Soman, T. Gu, Influence of surface roughness on microring-based phase shifters. IEEE Photonics Technol. Lett. **31**, 813–816 (2019)
32. M. Borselli, T.J. Johnson, O. Painter, Beyond the Rayleigh scattering limit in high-Q silicon microdisks: theory and experiment. Opt. Express **13**(5), 1515–1530 (2005)
33. X. Lu, A. McClung, K. Srinivasan, High-Q slow light and its localization in a photonic crystal microring. Nat. Photonics **16**, 66–71 (2022)
34. M.L. Gorodetsky, A.D. Pryamikov, V.S. Ilchenko, Rayleigh scattering in high-Q microspheres. JOSA B **17**, 1051–1057 (2000)
35. B.E. Little, J.-P. Laine, S.T. Chu, Surface-roughness-induced contradirectional coupling in ring and disk resonators. Opt. Lett. **22**, 4–6 (1997)
36. R. Huang, ŞK. Özdemir, J.-Q. Liao, F. Minganti, L.-M. Kuang, F. Nori, H. Jing, Exceptional photon blockade: engineering photon blockade with chiral exceptional points. Laser Photonics Rev. **16**, 2100430 (2022)
37. Y. Zuo, R. Huang, L.-M. Kuang, X.-W. Xu, H. Jing, Loss-induced suppression, revival, and switch of photon blockade. Phys. Rev. A **106**, 043715 (2022)
38. K. Ding, C. Fang, G. Ma, Non-Hermitian topology and exceptional-point geometries. Nat. Rev. Phys. **4**, 745–760 (2022)